Soft Matter

PAPER

View Article Online
View Journal

Cite this: DOI: 10.1039/d4sm00601a

Probing the physical origins of droplet friction using a critically damped cantilever†

Sankara Arunachalam, ‡ Marcus Lin ‡ and Dan Daniel *

Received 18th May 2024,
Accepted 2nd September 2024

DOI: 10.1039/d4sm00601a

rsc.li/soft-matter-journal

Previously, we and others have used cantilever-based techniques to measure droplet friction on various surfaces, but typically at low speeds $U < 1$ mm s^{-1}; at higher speeds, friction measurements become inaccurate because of ringing artefacts. Here, we are able to eliminate the ringing noise using a critically damped cantilever. We measured droplet friction on a superhydrophobic surface over a wide range of speeds $U = 10^{-5}$–10^{-1} m s^{-1} and identified two regimes corresponding to two different physical origins of droplet friction. At low speeds $U < 1$ cm s^{-1}, the droplet is in contact with the top-most solid (Cassie–Baxter), and friction is dominated by contact-line pinning with F_{fric} force that is independent of U. In contrast, at high speeds $U > 1$ cm s^{-1}, the droplet lifts off the surface, and friction is dominated by viscous dissipation in the air layer with $F_{fric} \propto U^{2/3}$ consistent with Landau–Levich–Derjaguin predictions. The same scaling applies for superhydrophobic and underwater superoleophobic surfaces despite their very different surface topographies and chemistries, *i.e.*, the friction scaling law derived here is universal.

1 Introduction

One conspicuous feature of wetting phenomena is the great diversity of timescales and contact-line speeds involved.[1–3] A typical millimetric water droplet sitting on a surface evaporates within an hour, which translates to the contact line retracting at a speed of ∼μm s^{-1};[4,5] in contrast, the same droplet bounces off a superhydrophobic surface within ∼ 10 ms with a contact-line speed of ∼ m s^{-1}.[6–8] To fully capture the wetting properties of a surface is therefore a daunting experimental task, requiring us to probe droplet friction—from the slowest to the fastest—over some 6 orders of magnitude.

Previously, we and others introduce cantilever-based techniques to measure droplet friction.[9–18] While the various techniques vary in their detailed implementations, they all rely on the same physical principle: a droplet (typically millimetric in size) is attached to a cantilever of known spring constant, and droplet friction can be determined by quantifying the cantilever deflection. Cantilever-based techniques have proven to be a simple but powerful tool to measure droplet friction with high sensitivity and precision (∼10 nN force resolutions[14–16]) over a wide range of surfaces—including superhydrophobic,[15,16] underwater superoleophobic,[14] and lubricated surfaces[12]—and with many advantages over traditional contact angle measurements.[2,19,20]

However, cantilever-based techniques are typically confined to low droplet speeds $U < 1$ mm s^{-1}. This is because at higher speeds, the cantilevers suffer from ringing artefacts resulting in inaccurate friction measurements. For example, see Fig. S2b in a recent publication by Backholm *et al.* (2024),[18] where ringing is clearly visible. In this work, we eliminate ringing by using a critically damped cantilever, greatly improving the measurement accuracy and signal-to-noise ratios at high speeds $U > 10$ cm s^{-1}; friction forces can also now be measured with the fastest theoretical time resolution of $1/\omega_o$, where ω_o is the natural frequency of the cantilever.

With our setup, we are able to measure droplet friction F_{fric} on superhydrophobic surfaces over an unprecedented range of speeds from 10 μm s^{-1} to 30 cm s^{-1}, spanning over 4 orders of magnitude. At low speeds $U < 1$ cm s^{-1}, F_{fric} is dominated by contact-line pinning and is independent of U, consistent with previous reports.[13,21] Here, we identify a new friction regime, where $F_{fric} \propto U^{2/3}$ for high $U > 1$ cm s^{-1} which can be attributed to viscous dissipation in the air layer, consistent with Landau–Levich–Derjaguin (LLD) formulations.[22,23] We further show that the derived scaling law is universal across different superhydrophobic and underwater superoleophobic surfaces.

Our approach to fabricating critically damped cantilevers—by enclosing the cantilever inside a column of viscous liquid (*e.g.*, water–glycerin mixture)—is simple to implement and can be used to probe the physical origins of droplet friction

Droplet Lab, Division of Physical Sciences and Engineering, King Abdullah University of Science and Technology (KAUST), Thuwal 23955–6900, Saudi Arabia. E-mail: danield@kaust.edu.sa

† Electronic supplementary information (ESI) available. See DOI: https://doi.org/10.1039/d4sm00601a

‡ These authors contributed equally to this work.

on various surfaces, uncovering the mechanisms behind different wetting phenomena.

2 Materials and methods

2.1 Surface preparations

Superhydrophobic Glaco samples were made by spray coating clean glass slides with a layer of hydrophobic nanoparticles (Glaco Mirror Coat Zero, Soft 99 Co). The samples were then placed vertically to dry for one hour before use, following the manufacturer's instructions. Black silicon surface was fabricated as described previously in the literature.[15,24] Scanning electron micrographs of the two surfaces can be found in Fig. 6A.

Underwater superoleophobic surfaces were prepared by grafting glass slides with zwitterionic poly(sulfobetaine methacrylate) brush surfaces. Details can be found in our previous publication.[14] Topography of the brush layer can be found in Fig. 6B as measuring using an atomic force microscope.

2.2 Contact angle measurements

Contact angle measurements were performed for 10 μL water drops using a commercially available instrument (Kruss DSA 100) at room temperature (21 °C, 60% humidity). To measure advancing and receding contact angles (θ_{adv} and θ_{rec}), water was pumped in and out at a rate of 0.2 μL s^{-1}. Results of the contact angle measurements are summarized in Table 1. Errors in the contact angle measurements $\delta\theta$ for the superhydrophobic surfaces are likely to be large. For $\theta = 175^\circ$, $\delta\theta$ can be as large as 5°, which translates to an error in $\Delta\cos\theta$ measurement of $\sqrt{2}\sin\theta\delta\theta \sim 10^{-2}$. As discussed in our previous work,[2] contact-line friction is better characterized by the quantity $\Delta\cos\theta = \cos\theta_{rec} - \cos\theta_{adv}$, rather than the more conventional $\Delta\theta = \theta_{adv} - \theta_{rec}$. Contact angle measurements cannot be done for an oil droplet on zwitterionic surface under water because it has contact angles of 180° and zero $\Delta\cos\theta$.[14]

2.3 Measuring friction

We used a cantilever-based method to measure the friction force F_{fric} acting on the droplet (Fig. 1A). Briefly, a water droplet (volume V = 15–30 μL) is attached by capillarity to cylindrical tubes (which act as cantilevers) of different dimensions, materials, and spring constants, as summarized in Table 2. The steel cylindrical tube is solid, while the acrylic tube is hollow with an inner diameter of 0.3 mm. Here, the droplet diameter $2R = (6V/\pi)^{1/3}$ = 3 mm is much larger than that of the cantilever $d < 0.4$ mm, such that the droplet geometry is minimally affected. At the same time, R is smaller than the capillary length of 2.7 mm, so that the droplet remains spherical.

Table 1 Properties of the superhydrophobic surfaces, where $\Delta\cos\theta = \cos\theta_{rec} - \cos\theta_{adv}$

Surface	θ_{adv}	θ_{rec}	$\Delta\cos\theta$
Glaco	172°	168°	1.2×10^{-2}
Black silicon	174°	170°	1.0×10^{-2}

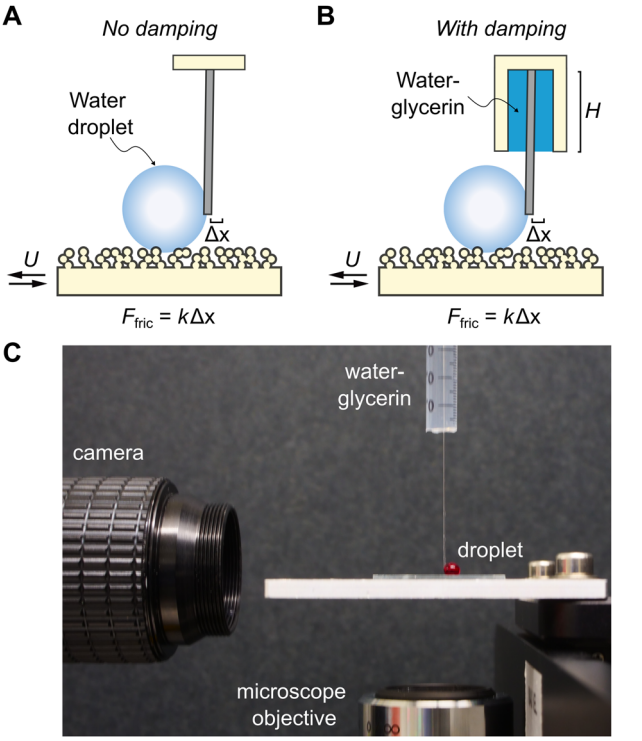

Fig. 1 Droplet force apparatus (DFA). Schematic of instrument used to measure droplet friction on superhydrophobic surface (A) without damping and (B) with damping. (C) Photograph of DFA setup with damping. Food dye is added to the water droplet for clarity, but it is not used in our experiments.

Table 2 Cantilever/cylindrical tube properties. d is the tube outer diameter, L is its length, k the spring constant, and b_0 the intrinsic damping coefficient without any liquid column, *i.e.*, in air

Material	d (mm)	L (cm)	k (mN m^{-1})	b_0 (mg s^{-1})
Acrylic	0.36	9	14	47 ± 5
Acrylic	0.36	6	55	105 ± 20
Steel	0.15	5.5	144	49 ± 5

The surface was moved back-and-forth at a controlled speed of $U = 10^{-5}$–10^{-1} m s^{-1} using a motorized stage. F_{fric} can then be inferred from the cantilever deflection Δx (averaged over several cycles), since $F_{fric} = k\Delta x$ where k = 14–144 mN m^{-1} is the flexular spring constant. Δx was recorded using a high speed camera (up to 1000 fps, Krontech Chronos 2.1) and determined using a cross-correlation algorithm with micron resolutions. The entire setup was placed on an optical table and enclosed to minimise vibration and draught. This way, we can reduce the inherent instrument noise to ΔF_{noise} = 5 nN and reliably measure forces as small as 10 nN. The inherent ΔF_{noise} is obtained by measuring cantilever deflection in absence of any droplet motion.

We previously named this custom-built instrument the Droplet Force Apparatus (DFA),[14] whose details can be found in our previous publications.[12–14] An important innovation we introduced here is the addition of a damping system. We placed the cantilever coaxially inside a cylinder (with a much

larger radius of 2.5 mm) filled with water–glycerin solution (Fig. 1B). By optimizing the glycerin concentration (and hence the liquid column viscosity η_c) and liquid column height H, we can achieve a critically damped system and measure F_{fric} with the fastest theoretical time resolution of $1/\omega_o$, where $\omega_o = \sqrt{k/m}$ is the natural frequency of the cantilever with an attached droplet of mass m. Critical damping is achieved when $b = \sqrt{4mk}$, *i.e.*, the damping coefficient has to be tuned for specific droplet-cantilever combination for particular droplet mass m and the spring constant k. Here, the cantilever masses are much smaller than m and can be safely ignored.

The DFA setup can also be integrated with microscopy (specifically reflection interference contrast microscopy) to visualize the droplet base as shown in Fig. 1C.

2.4 Measuring cantilever spring constant

The spring constant of the cantilever k can be determined using the added weight method.[12,21] We placed masses (*e.g.*, microlitre-sized water droplets) of different weights W at the cantilever tip and measured the deflection Δz optically. The slope of W *vs.* Δz corresponds to k. k can also be obtained from the natural frequency ω_o. See details in Fig. S1, S2 and Table S1 (ESI†).

2.5 Measuring damping coefficient b from free-decay oscillations

To measure the damping coefficient, we attached a solid mass with m = 25–270 mg to the cantilever. We then applied a short impulse by blowing air to the attached mass using a blower ball. As long as $b/\sqrt{4mk} < 1$, the mass will perform an under-damped simple harmonic motion with an exponential decay envelope $\exp(-bt/(2m))$, from which we can derive b.

2.6 Visualizing droplet base

We used reflection interference contrast microscopy (RICM) to visualize the droplet base and the air film beneath it.[12,14,25] Briefly, we shone monochromatic light (wavelength λ = 561 nm) from below and captured the reflection off the droplet's base using a high-speed camera (Photron Nova S20) fitted with a 5× microscope objective. The air film gives rise to thin-film interference, *i.e.*, dark and bright fringes as the light reflected off the water–air and air–solid interfaces interfere destructively and constructively with one another. Contact-line pinning (including its absence) can be clearly observed using this technique.

3 Results and discussions

3.1 Ringing artefact in underdamped cantilever

We start by measuring droplet friction without the addition of any damping system on our custom-built instrument, which we named the droplet force apparatus or DFA (Fig. 1A). Fig. 2A shows a typical force curve for a 25 μL water droplet (mass m = 25 mg) moving back and forth on a Glaco superhydrophobic surface at a controlled speed of U = 0.1 mm s^{-1} (3 cycles over a D = 5 mm distance). In this case, DFA is able to accurately measure the friction force F_{fric} = 1.0 ± 0.1 μN (Fig. 2A). At this low speed, the droplet is in contact with the topmost solid fractions, and the observed force fluctuations $\Delta F_{contact}$ = 0.1 μN (inset in Fig. 2A) can be attributed to contact-line pinning at the receding edge (Video S1, ESI†) and is significantly larger than the inherent instrument noise ΔF_{noise} = 5 nN; $\Delta F_{contact}$ reflects the topographical heterogeneity of superhydrophobic surfaces, *i.e.*, it is not an experimental artefact or noise.

In contrast, the observed force fluctuations ΔF_{Gibbs} at higher speeds U = 10 and 30 cm s^{-1} are Gibbs ringing noise, an experimental artefact that should be eliminated (Fig. 2B and C). ΔF_{Gibbs} oscillates at frequency $\omega_o \approx$ 20 rad s^{-1} and is associated with the failure of the underdamped cantilever to respond quickly enough to the droplet inertia ma, where m and a are the droplet's mass and acceleration. For U = 10–30 cm s^{-1} (Fig. 2B and C), $ma \sim mU\omega_o \approx$ 50–120 μN, much larger than F_{fric} = 1 μN, and we therefore observed Gibbs noise. In contrast, for U = 0.1 mm s^{-1} (Fig. 2A), $mU\omega_o \approx$ 50 nN $\ll F_{fric}$, and there was no Gibbs noise.

For U = 10 cm s^{-1}, the initial ΔF_{Gibbs} = 1.3 μN and is comparable to the actual friction force F_{fric} = 1.9 μN. Fortunately, ΔF_{Gibbs} decays within a couple of seconds to allow for reasonably accurate F_{fric} measurement. The ringing noise is exacerbated at an even higher U = 30 cm s^{-1} with ΔF_{Gibbs} = 3.7 μN, again comparable

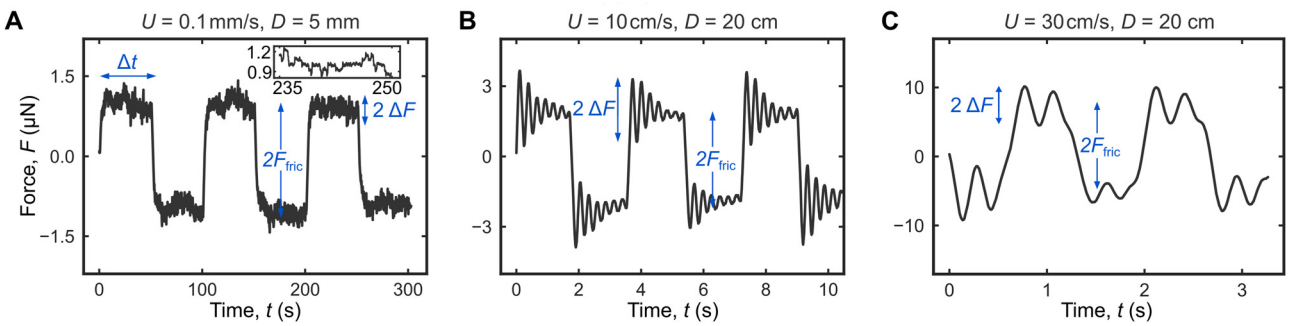

Fig. 2 Ringing artefact in droplet friction measurements (without damping). Friction force measurements are performed for 3 back-and-forth cycles at different speeds for a fixed droplet volume of 25 μL. (A) At low speed U = 0.1 mm s^{-1}, the observed ΔF is due to contact-line pinning. (B) At high speed U = 10 cm s^{-1}, ΔF is primarily due to ringing artefact which decays with time. (C) At an even higher U = 30 cm s^{-1}, ringing is even more prominent, and there is insufficient time for the noise to decay down. During every cycle, the travel distance each way are $D = U\Delta t$ = 5 mm for (A), 20 cm for (B) and (C); these distances are many times the size of the water droplet.

to F_{fric} = 7.0 μN. However, this time ΔF_{Gibbs} does not decay quickly enough and adversely impact the accuracy of friction measurements.

The required travel distance $D = U\Delta t$ quickly rises with increasing U. F_{fric} can be accurately measured with D = 5 mm when U = 0.1 mm s^{-1} (Fig. 2A). However, when U = 30 cm s^{-1}, friction measurements remain challenging even with D = 20 cm (Fig. 2C). Without any damping system, friction measurements at high speeds are impossible for small sample sizes ~ 1 cm. In the next section, we will discuss how these limitations can be overcome by using a critically damped cantilever.

3.2 Designing critically damped cantilever

The damping coefficient b of the cantilevers can be obtained by observing the free decay oscillation of an attached solid mass m following a short impulse (Fig. 3A). For an underdamped system where $b/\sqrt{4mk} \ll 1$, the cantilever oscillates close to the natural frequency $\omega_o = \sqrt{k/m}$, which was observed experimentally for a wide range of k = 14–144 mN m^{-1} and m = 25–270 mg (Fig. 3B). We also expect the oscillations to dampen with a decay envelope of the form $e^{-bt/(2m)}$, which was also borned out by experiments (Fig. 3C and D).

The damping coefficient $b = b_0 + b_\eta$ has two components b_0 and b_η. b_0 is the intrinsic damping coefficient, whose physical origin is complex but is linked to the dissipation at the fixed point of the cantilever mounted to the top wall. Experimentally, b_0 can be obtained from the decay envelope in air (no liquid column). For the cantilever with k = 14 mN m^{-1}, we obtained b_o = 55 mg s^{-1} (Fig. 3C, Top). On the other hand, b_η is the viscous component due to the liquid column, whose magnitudes can be tuned by changing the liquid column viscosity η_c (Fig. 3C) and/or the column height H (Fig. 3D). This allows us to continuously tune b from its intrinsic value of 55 mg s^{-1} (Fig. 3C, Top) to a maximum value of 815 mg^{-1} (Fig. 3D, bottom).

Fig. 3E summarizes the experimental b values for three different cantilevers (see Table 2 for detailed properties) as we vary the liquid column height H = 0–4.5 cm and viscosities η_c = 9, 81 mPa s. When $b_\eta = b - b_0$ is normalized by $\eta_c d$ (where d is the cantilever diameter) and H normalized by the cantilever length L, the data in Fig. 3E collapse into a single master curve (Fig. 3F) that is well-described by the power law

$$b_\eta/(\eta_c d) = 810(H/L)^{4.43} \quad (1)$$

We then used eqn 1 to optimize H and η_c to achieve critical damping, *i.e.*, $b = \sqrt{4mk}$. Since there are 5 variables (b_η, η_c, d, H, and L) and 3 fundamental dimensions (mass, length, and time), Buckingham π theorem guarantees that there can only be 5–3 = 2 dimensionless groups, which we have chosen here to be $b_\eta/(\eta_c d)$ and H/L. The fact that $b_\eta/(\eta_c d)$ scales with H/L suggests that the hydrodynamic damping is primarily due to Stokes flow in the liquid column, *i.e.*, low Reynolds number flow;[26] this is contrast to damping in atomic force microscope cantilevers where it is dominated by high Reynolds number flow.[27] To rigorously justify the empirical fit in eqn 1 requires significant mathematical modelling outside the scope of this study.

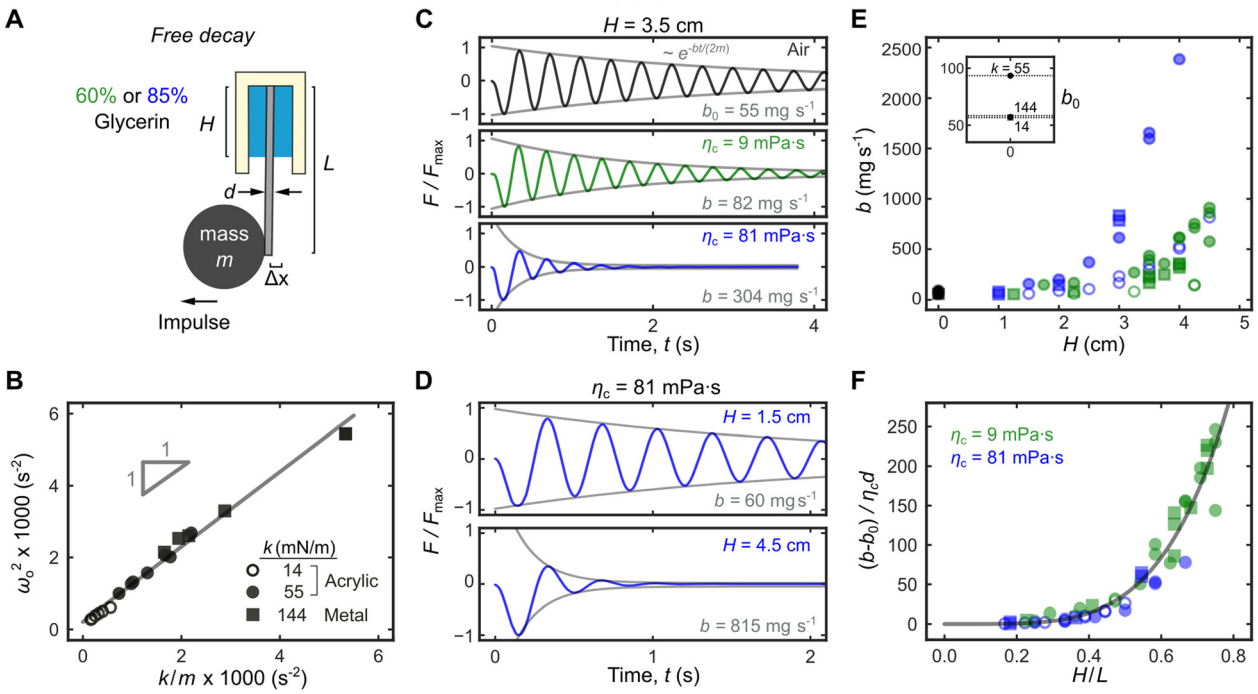

Fig. 3 Tuning the damping system in DFA. (A) The damping coefficient b can be measured by observing the free decay oscillation of an attached mass m following an impulse. (B) The oscillation frequency ω_o (in air) depends on the spring constant k and the attached mass m. For the same cantilever, b can be tuned by changing (C) the viscosity of the liquid column η_c and/or (D) the column height H. (E) b as a function of H for different cantilevers and liquid column viscosities (indicated by different markers and colours, respectively). Inset shows the damping coefficient b_0 when H = 0, *i.e.*, in air. (F) When correctly normalized, data in E collapse into a single master curve in eqn (1) (gray line).

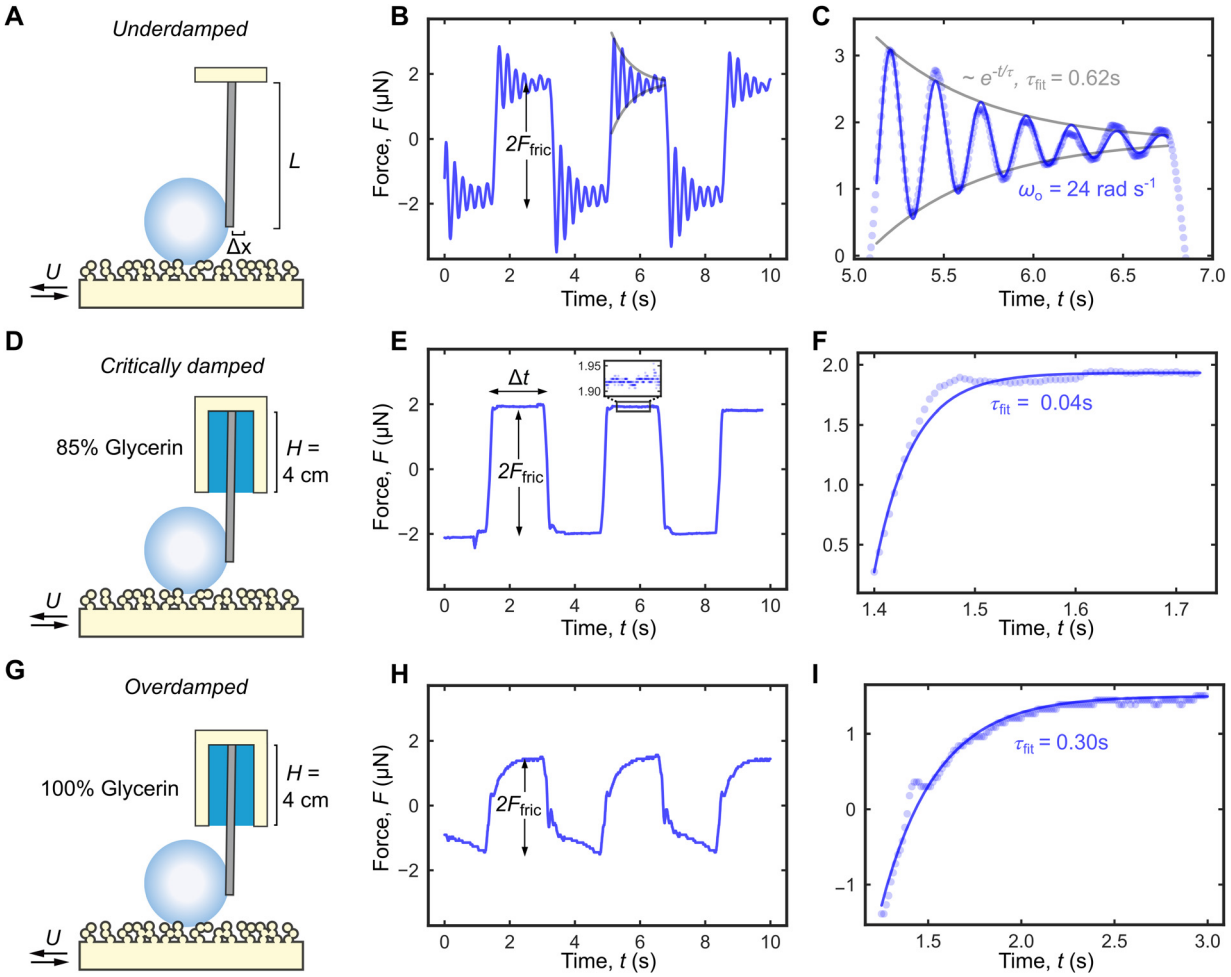

Fig. 4 Cantilever systems with different dampings. We measured friction F_{fric} for 20 μL droplets at a fixed speed of 10 cm s^{-1}. (A) When using a cantilever (k = 14 mN m^{-1}) with no added damping, the system is underdamped, (B) and the force curve has the characteristic ringing artefact with (C) a decay time τ = 0.62 s. (D) When filled with H = 4 cm of 85% glycerin mixture, the system is close to critically damped. (E) There is no ringing artefact, (F) and the system has a response time close to the theoretical maximum $\tau = 1/\omega_0$. (G) When replaced with 100% glycerin, the system is overdamped. (H) There is no ringing noise, (I) but the response time τ = 0.3 s is significantly larger than $1/\omega_0$.

To illustrate the importance of using a critically damped cantilever, we performed friction measurements at a relatively high U = 10 cm s^{-1} using the same droplet volumes (V = 20 μL and m = 20 mg) and cantilever (k = 14 mN m^{-1} and $\omega_o = \sqrt{k/m} = 24$ rad s^{-1}), but with three different damping coefficients b = 50, 700, 7000 mg s^{-1} corresponding to underdamped, critically damped (or nearly so), and overdamped cases (Fig. 4). The underdamped case is just a cantilever with no liquid column, while the critically damped and overdamped cases are achieved by enclosing the cantilever with 85% and 100% glycerin of column height H = 4 cm. $b/\sqrt{4mk}$ = 0.04, 0.7, and 7 for the three cases (Table 3), and the travel distance $D = U\Delta t$ is fixed at 20 cm.

The droplet-cantilever system can be modelled as a simple harmonic oscillator, and in the underdamped case (Fig. 4A–C), we expect significant ringing artefact described by the force response function

$$F(t) = F_0 e^{-t/\tau}\cos(\omega_o t + \phi) + F_{fric} \quad \text{for} \frac{b}{\sqrt{4mk}} \ll 1 \qquad (2)$$

Table 3 Experimental parameters and results in Fig. 4. b is calculated using eqn 1. The droplet mass m = 20 mg and the spring constant k = 14 mN m^{-1} in all experiments. Error in F_{fric} is based on standard deviation for the last 0.5 second of the force curve

Cases	b (mg s^{-1})	$b/\sqrt{4mk}$	τ_{theor} (s)	τ_{fit} (s)	F_{fric} (μN)
A–C	50	0.04	$2m/b$ = 0.8	0.62	1.7 ± 0.2
D–F	700	0.7	$1/\omega_o$ = 0.037	0.04	1.93 ± 0.01
F–H	7000	7	b/k = 0.5	0.3	1.50 ± 0.01

with a decay/response time of $\tau = 2m/b$, and where F_0 and the phase ϕ are fitting parameters that depend on initial conditions (see Fig. S3 for detailed derivation, ESI†). The experimental force curve in Fig. 4C (blue circles) is well described by eqn 2 (blue line) with a fitted response time τ_{fit} = 0.62 s that is in good agreement with the theoretical value of $2m/b$ = 0.8 s (Table 3). Discrepancy between the two is likely due to uncertainty in b value.

In contrast, for a system close to critically damped (Fig. 4D–F), there is no ringing and $F(t)$ has the form

$$F(t) = F_0 e^{-t/\tau} + F_{fric} \quad \text{for} \frac{b}{\sqrt{4mk}} \approx 1 \qquad (3)$$

reaching the F_{fric} = 1.9 μN value with the fastest possible time $\tau = 1/\omega_o$. The experimental force curve in Fig. 4F (blue circles) is again well fitted with eqn 3 (blue line), with τ_{fit} = 0.04 s that is in excellent agreement with expected $1/\omega_o$ = 0.037 s. The initial overshoot of the experimental data (with respect with theoretical predictions) is due to the fact that the system is slightly underdamped $b/\sqrt{4mk} = 0.7$. Physically, critical damping is achieved when the droplet inertia is balanced by the viscous component: $mU\omega_o \sim bU$ and hence $b \sim \sqrt{mk}$.

For an overdamped system (Fig. 4G–I), the force response function has a similar form to the critically damped one

$$F(t) = F_0 e^{-t/\tau} + F_{fric} \quad \text{for} \frac{b}{\sqrt{4mk}} \gg 1 \qquad (4)$$

except with a larger $\tau = b/k$. Fitting the experimental data in Fig. 4I (blue circles) with Eqn 4 gives τ_{fit} = 0.3 s $\gg 1/\omega_o$ and in good agreement with the expected value of b/k = 0.5 s.

We obtained similar friction values for undamped and critically damped cantilevers: F_{fric} = 1.7 ± 0.2 μN and F_{fric} = 1.93 ± 0.01 μN, respectively. In contrast, F_{fric} = 1.50 ± 0.01 μN is significantly smaller with overly damped cantilever, likely because there is insufficient time for F_{fric} to reach its equilibrium value (Table 3). The advantages to using a critically damped cantilever are therefore clear. F_{fric} can be accurately measured with minimal ΔF, since ringing artefact can be avoided, and the cantilever responds with the fastest theoretical time possible.

3.3 Probing different origins of droplet friction on superhydrophobic surfaces

Using a critically damped cantilever, we are now able to measure F_{fric} over an unprecedented range of U from 10 μm s^{-1} to 30 cm s^{-1} without any Gibbs noise. We identified two regimes of droplet frictions at low and high speeds. At low U < 1 cm s^{-1}, F_{fric} is independent of U, and there is significant fluctuations ΔF = 0.2 μN in the force curve (inset in Fig. 4B). In contrast, at high U > 10 cm s^{-1}, $F_{fric} \propto U^{2/3}$ increases with U, and the force curve exhibits ultra-low ΔF < 10 nN (inset in Fig. 5C).

To explain the physical origins of the two regimes, we shone monochromatic light (wavelength λ = 561 nm) from below to visualize the droplet base, *i.e.*, reflection interference contrast microscopy (RICM). At low U = 0.1 mm s^{-1}, a droplet is in contact with the topmost tips of the surface (Cassie–Baxter state). Roughness of the superhydrophobic surface results in variations in the air film thickness beneath the droplet, which manifest as bright and dark fringes due to interference effects (Fig. 5D). Between neighbouring bright and dark fringes, there is a difference in air-film thickness of $\sim\lambda/2$ or 200 nm (Fig. S4A, ESI†).

In this regime, F_{fric} (and the observed $\Delta F_{contact}$ = 0.2 μN in Fig. 5B) is attributed to contact-line pinning, resulting in discontinuous contact-line profile at the receding end (Video S1, ESI†). Furmidge's law predicts that F_{fric} is directly related to contact angle hysteresis, specifically that $F_{fric}/2r\gamma = \Delta\cos\theta = \cos\theta_{rec} - \cos\theta_{adv}$, where r is droplet base radius and γ the surface tension.

On the other hand, at high speeds U > 10 cm s^{-1}, droplet motion can generate sufficient lift to balance its weight, and the the droplet completely lifts off the surface.[28–30] There is no contact-line pinning, and as a result, the droplet base profiles at both the advancing front and receding end are smooth and continuous (Fig. 5E, Fig. S4B and Videos S2–S4, ESI†), with the characteristic horseshoe shape as described in previous reports.[30] Contact angle measurements can no longer describe

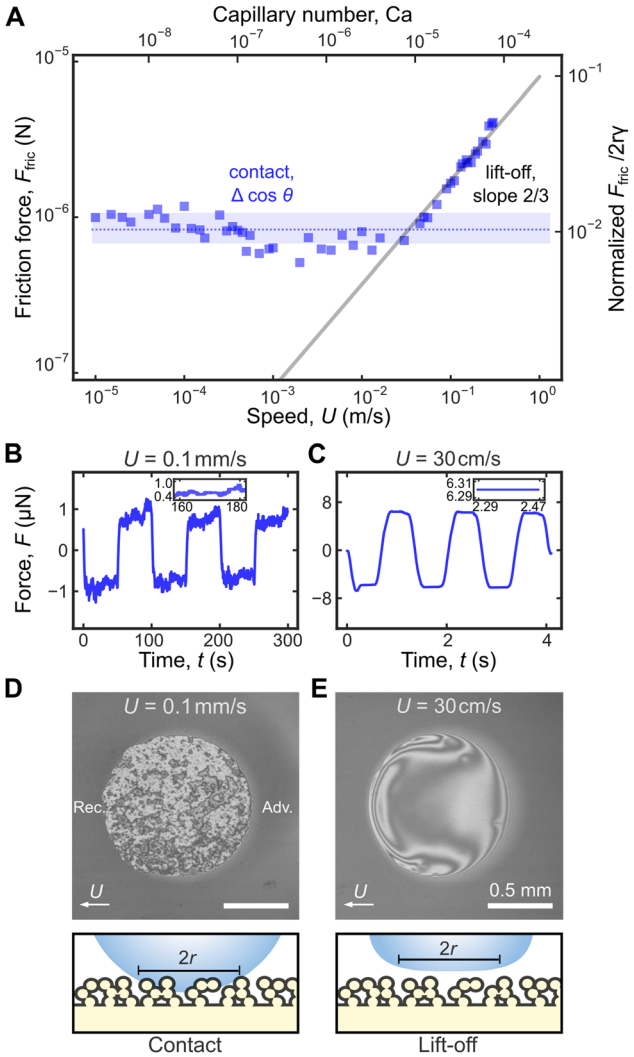

Fig. 5 Origins of droplet friction probed using a critically damped cantilever. (A) Friction force F_{fric} as a function of speed U. Secondary x and y axes are U and F_{fric} in their non-dimensional form. Droplet volume is 20 μL. (B) and (C) The corresponding force curves for at low U = 0.1 mm s^{-1} and high U = 30 cm s^{-1}. Droplet base visualized using reflection interference contrast microscopy. (D) At low U = 0.1 mm s^{-1}, droplet is in contact with the topmost solid fractions. The advancing (Adv.) front and the receding (Rec.) ends are indicated on the image. (E) At high U = 30 cm s^{-1}, the droplet lifts off the surface. Arrows indicate motion of the surface. Scale bars for D and E are 0.5 mm.

droplet friction in this limit, since there is no three-phase contact line. The lack of contact-line pinning due to droplet lift-off explains the ultra-low $\Delta F = \Delta F_{noise} < 10$ nN (inset in Fig. 5C) in the force curve. Note that without damping, the force curve is dominated by Gibbs noise (Fig. 2C), and we will not be able to come to this conclusion.

Instead, friction is dominated by the viscous dissipation in the air layer whose thickness h increases with U. Following the classical analysis by Landau, Levich, and Derjaguin,[22,23] $h \propto R\mathrm{Ca}^{2/3}$, where $\mathrm{Ca} = \eta U/\gamma$ is the capillary number based on the air viscosity $\eta = 1.85 \times 10^{-5}$ Pa s and the surface tension of water $\gamma = 72$ mN m^{-1}. Viscous dissipation occurs largely in the perimeter of the droplet base of size $l \propto R\mathrm{Ca}^{1/3}$, and we expect $F_{fric} \sim 2rl(\eta U/h)$ and hence $F_{fric}/2r\gamma \sim \mathrm{Ca}^{2/3} \propto U^{2/3}$ (full line in Fig. 5A). Recently, Backholm *et al.* (2024) reported a similar increase of F_{fric} with U on superhydrophobic surfaces and proposed that $F_{fric} \propto U$; however, $F_{fric} \propto U^{2/3}$ gives a better fit to their experimental data (Fig. S5, ESI†).

4 Universal droplet friction laws for super-repellent surfaces

In Fig. 5, we only looked at friction for water droplets (viscosity $\eta_d = 10^{-3}$ Pa s) of a fixed volume $V = 20$ μL on a Glaco superhydrophobic surface which has a porous texture consisting of nanoparticles (Fig. 6A). In Fig. 6, we additionally measured F_{fric} for a wider range of volumes $V = 15$–30 μL not just for Glaco surface, but also for black silicon, a different superhydrophobic surface with needle-like structures. We have also included previously published friction data for silicone oil droplets ($V = 20$–50 μL and of much higher viscosity $\eta_d = 10^{-1}$ Pa s) on underwater superoleophobic surface for comparison.[14] Unlike superhydrophobic surface, the underwater superoleophobic surface is smooth at the nanoscale and does not rely on texturing to achieve liquid-repellency (Fig. 6B); instead, the zwitterionic brushes on the surface generate electric double-layer forces which stabilize a water layer beneath the oil droplet.

The entire friction dataset in Fig. 6C spans a wide range of F_{fric} (close to 3 decades, from 20 nN to 6 μN) and droplet speeds (over 4 decades, from 10 μm s^{-1} to 30 cm s^{-1}). The same data can be presented in their non-dimensionalized form $F_{fric}/2r\gamma$ *vs.* Ca as shown in Fig. 6D (raw data in[31]). For the zwitterionic surface, we use the water–oil interfacial tension $\gamma = 50$ mN m^{-1} and the water viscosity $\eta = 10^{-3}$ Pa s values to calculate Ca (*c.f.*, water surface tension $\gamma = 72$ mN m^{-1} and air viscosity $\eta = 1.8 \times 10^{-5}$ Pa s for superhydrophobic surface). Parameters used to generate the non-dimensional plot is summarized in Table 4.

As discussed previously, there are two regimes of droplet friction, one dominated by contact-line pinning and another by viscous dissipation

$$F_{fric}/2r\gamma = \begin{cases} \Delta\cos\theta & \text{contact-line pinning} \\ 20\,\mathrm{Ca}^{2/3} & \text{viscous dissipation} \end{cases} \quad (5)$$

For Glaco surface, contact-line pinning dominates for $U < 10$ cm s^{-1} and $\mathrm{Ca} < 10^{-5}$ with constant $F_{fric}/2r\gamma = (1.0 \pm 0.1) \times 10^{-2}$ (blue band in Fig. 6D). For black silicon, pinning is dominant for smaller $U < 1$ cm s^{-1} and $\mathrm{Ca} < 10^{-6}$, with a lower $F_{fric}/2r\gamma = (8 \pm 2) \times 10^{-4}$ (red band in Fig. 6D), reflecting its more water-repellent nature. It is difficult to directly compare friction and contact angle measurements to confirm Furmidge's law, because of large measurement error for $\theta > 170^\circ$ (see discussion in 'Contact angle measurements' subsection in 'Materials and methods'). Previously, we showed that for an oil droplet moving on zwitterionic brush surface, the droplet is never in contact with the solid and contact-line pinning is always absent. Hence, there is no constant $F_{fric}/2r\gamma$ regime.

Above critical speeds corresponding to $\mathrm{Ca} = 10^{-5}$ and 10^{-6} for Glaco and black silicon, the water droplet lifts off the surface and viscous dissipation in the air layer dominates with

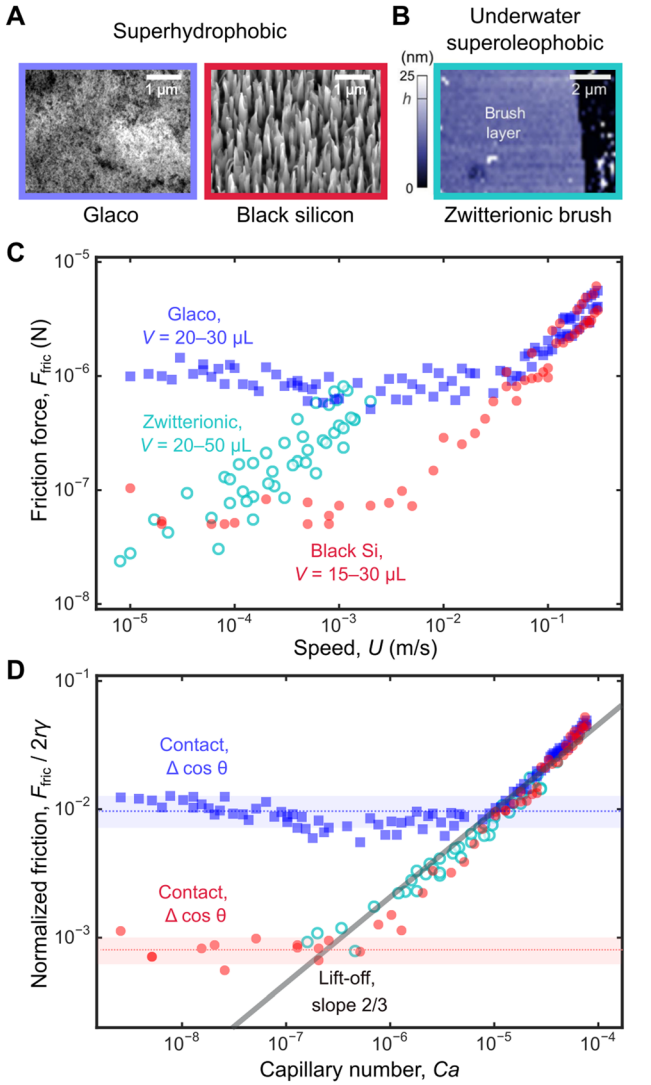

Fig. 6 Universal friction laws on different surfaces. (A) Scanning electron micrographs of Glaco and black silicon superhydrophobic surfaces. (B) Topography of the zwitterionic brush layer (in water) obtained using atomic force microscope. On the right, the brush layer has been scratched to reveal the underlying glass surface. (C) Friction forces measured for the three surfaces over a wide range of speeds from 10 μm s^{-1} to 30 cm s^{-1}. (D) The same data in C non-dimensionalized as $F_{fric}/2r\gamma$ *vs.* Ca. Data for zwitterionic brush surface is taken from our previous work.[14]

Table 4 Experimental parameters in Fig. 6

Surface	Droplet (Pa s)	Outside	Droplet viscosity, η_d (Pa s)	Outside viscosity, η (Pa s)	γ (mN m^{-1})
Glaco	Water	Air	10^{-3}	1.8×10^{-5}	72
Black Si	Water	Air	10^{-3}	1.8×10^{-5}	72
Zwitterionic	Oil	Water	10^{-1}	1.0×10^{-3}	50

$F_{fric}/2r\gamma = 20\ Ca^{2/3}$ (full line in Fig. 6D, prefactor of 20 obtained by least squares fit to data) independent of the surface structure. There is excellent overlap between friction data for oil droplets on zwitterionic surface and for water on superhydrophobic surfaces, even though the droplet viscosities are very different (η_d is 100 times larger for oil than for water), *i.e.*, dissipation due to internal flow of droplet is insignificant. Instead, F_{fric} on zwitteronic surface is always dominated by viscous dissipation in the water layer beneath the oil droplet, due to the same LLD droplet lift-off mechanism.

The scaling law in eqn (5) is therefore universal, and the $Ca^{2/3}$ scaling applies equally to superhydrophobic and underwater superoleophobic surface, despite their very different surface topographies and chemistries. At even higher speeds $\sim$ m s^{-1}, other dissipation mechanisms, such as aerodynamic drag can become important.[32] However, since droplet speeds here $U \leq 30$ cm s^{-1} are relatively low, the drag force $F_{drag} \sim \rho_a R^2 U^2/Re^{1/2} \sim 20$ nN is small and therefore unimportant. $Re = \rho_a UR/\eta < 30$ is the Reynolds number, ρ_a and η are the air density and viscosity, and R is the droplet radius.

5 Conclusions

To conclude, we have proposed a design for a critically damped cantilever which allows us measure droplet frictions accurately at high speeds without any ringing artefacts. We are able to then identify a new droplet friction regime on superhydrophobic surfaces where $F_{fric}/2r\gamma \sim Ca^{2/3}$ at high speeds. We further showed that this scaling is universal and remains true for both superhydrophobic and underwater superoleophobic surface, irrespective of the details of surface structure and chemistry.

Author contributions

S. A. performed the bulk of the experiments. D. D. and M. L. came up with the design of the critically damped cantilever, analyzed the results, and wrote the manuscript. D. D. conceptualized the project and supervised the research.

Data availability

Data for this article, including dataset for friction measurements are available at Harvard Dataverse at **https://doi.org/10.7910/DVN/2J4ZTP**.

Conflicts of interest

There are no conflicts to declare.

Acknowledgements

This work was supported by KAUST start-up fund BAS/1/1416-01-01.

Notes and references

1 P.-G. de Gennes, *Rev. Mod. Phys.*, 1985, **57**, 827.
2 D. Daniel, M. Vuckovac, M. Backholm, M. Latikka, R. Karyappa, X. Q. Koh, J. V. I. Timonen, N. Tomczak and R. H. A. Ras, *Commun. Phys.*, 2023, **6**, 152.
3 P.-G. Gennes, F. Brochard-Wyart and D. Quéré, *Capillarity and wetting phenomena: drops, bubbles, pearls, waves*, Springer, 2004.
4 R. G. Picknett and R. Bexon, *J. Colloid Interface Sci.*, 1977, **61**, 336–350.
5 D. Brutin and V. Starov, *Chem. Soc. Rev.*, 2018, **47**, 558–585.
6 D. Richard, C. Clanet and D. Quéré, *Nature*, 2002, **417**, 811.
7 Y. Liu, L. Moevius, X. Xu, T. Qian, J. M. Yeomans and Z. Wang, *Nat. Phys.*, 2014, **10**, 515–519.
8 J. C. Bird, R. Dhiman, H.-M. Kwon and K. K. Varanasi, *Nature*, 2013, **503**, 385–388.
9 H.-J. Butt, I. V. Roisman, M. Brinkmann, P. Papadopoulos, D. Vollmer and C. Semprebon, *Curr. Opin. Colloid Interface Sci.*, 2014, **19**, 343–354.
10 H. Suda and S. Yamada, *Langmuir*, 2003, **19**, 529–531.
11 D. W. Pilat, P. Papadopoulos, D. Schäffel, D. Vollmer, R. Berger and H.-J. Butt, *Langmuir*, 2012, **28**, 16812–16820.
12 D. Daniel, J. V. I. Timonen, R. Li, S. J. Velling and J. Aizenberg, *Nat. Phys.*, 2017, **13**, 1020–1025.
13 D. Daniel, J. V. I. Timonen, R. Li, S. J. Velling, M. J. Kreder, A. Tetreault and J. Aizenberg, *Phys. Rev. Lett.*, 2018, **120**, 244503.
14 D. Daniel, A. Y. T. Chia, L. C. H. Moh, R. Liu, X. Q. Koh, X. Zhang and N. Tomczak, *Commun. Phys.*, 2019, **2**, 105.
15 M. Backholm, D. Molpeceres, M. Vuckovac, H. Nurmi, M. J. Hokkanen, V. Jokinen, J. V. I. Timonen and R. H. A. Ras, *Commun. Mater.*, 2020, **1**, 1–8.
16 M. Hokkanen, M. Backholm, M. Vuckovac, Q. Zhou and R. H. A. Ras, *Adv. Mater.*, 2021, **33**, 2105130.
17 C. Hinduja, A. Laroche, S. Shumaly, Y. Wang, D. Vollmer, H.-J. Butt and R. Berger, *Langmuir*, 2022, **38**, 14635–14643.
18 M. Backholm, T. Kärki, H. A. Nurmi, M. Vuckovac, V. Turkki, S. Lepikko, V. Jokinen, D. Quéré, J. V. I. Timonen and R. H. A. Ras, *Proc. Natl. Acad. Sci. U. S. A.*, 2024, **121**, e2315214121.
19 A. Marmur, *Annu. Rev. Mater. Res.*, 2009, **39**, 473–489.
20 K. Liu, M. Vuckovac, M. Latikka, T. Huhtamäki and R. H. A. Ras, *Science*, 2019, **363**, 1147–1148.
21 M. Backholm and O. Bäumchen, *Nat. Protoc.*, 2019, **14**, 594–615.

22 L. Landau and V. Levich, *Acta Physicochim. USSR*, 1942, **17**, 42–54.
23 B. Derjaguin, *Dokl. Acad. Sci. USSR*, 1943, **39**, 13–16.
24 L. Sainiemi, V. Jokinen, A. Shah, M. Shpak, S. Aura, P. Suvanto and S. Franssila, *Adv. Mater.*, 2011, **23**, 122–126.
25 L. Limozin and K. Sengupta, *Chem. Phys. Chem.*, 2009, **10**, 2752–2768.
26 G. A. Cranch, J. E. Lane, G. A. Miller and J. W. Lou, *J. Appl. Phys.*, 2013, **113**, 194904.
27 J. E. Sader, *J. Appl. Phys.*, 1998, **84**, 64–76.
28 H. Lhuissier, Y. Tagawa, T. Tran and C. Sun, *J. Fluid Mech.*, 2013, **733**, R4.
29 A. Gauthier, J. C. Bird, C. Clanet and D. Quéré, *Phys. Rev. Fluids*, 2016, **1**, 084002.
30 E. Sawaguchi, A. Matsuda, K. Hama, M. Saito and Y. Tagawa, *J. Fluid Mech.*, 2019, **862**, 261–282.
31 D. Daniel, Raw friction data, Harvard Dataverse, 2024, DOI: **10.7910/DVN/2J4ZTP**.
32 T. Mouterde, P. S. Raux, C. Clanet and D. Quéré, *Proc. Natl. Acad. Sci. U. S. A.*, 2019, **116**, 8220–8223.